Korea-Australia Rheology Journal
Vol. 20, No. 3, September 2008 pp. 153-164

Nanofibers from electrically driven viscoelastic jets: modeling and experiments

Colman P. Carroll, Eduard Zhmayev, Vibha Kalra and Yong Lak Joo
School of Chemical & Biomolecular Engineering, Cornell University, Ithaca, NY, 14853
(Received May 6, 2008)

Abstract

Modeling and experiments of three electrospinning systems have been presented and they are i) axisymmetric instabilities in electrospinning of various polymeric solutions, ii) non-isothermal modeling of polymer melt electrospinning, and iii) control of nanoparticle distribution and location via confined self-assembly of block copolymers during electrospinning. It has been demonstrated that predicted simulations are in good agreement with corresponding electrospinning experiments, and theoretical analysis provides fundamental understanding of phenomena that take place during electrospinning of various polymeric liquids.

Keywords : electrospinning, axisymmetric instability, nonisothermal modeling, block copolymer nanocomposites

1. Introduction

Electrostatic fiber spinning or 'electrospinning' is a unique process for forming fibers with submicron scale diameters through the action of electrostatic force (Fong and Reneker, 2001). The resulting nanofibers are collected as non-woven mats with extremely large surface to mass ratios, which can be used in filtration, catalysis, and biomedical applications (Huang *et al.*, 2003). Studies in electrospinning, however, have mostly been lead by experimental approaches, and comprehensive comparison between theory and experiments is rare. The current communication focuses on some recent work on comprehensive modeling and its validation via experiments. Three systems will be presented and they are i) axisymmetric instabilities in electrospinning of various polymeric solutions, ii) non-isothermal modeling of polymer melt electrospinning, and iii) control of nanoparticle distribution and location via confined self-assembly of block copolymers during electrospinning. It will be demonstrated that predicted simulations are in good agreement with corresponding electrospinning experiments and theoretical analysis provides fundamental understanding of phenomena that take place during electrospinning of various polymeric liquids.

2. Axisymmetric instability during electrospinning of highly conducting, viscoelastic solutions

Generally it is desirable to obtain smooth, uniform fiber in electrospinning, however, in some cases it is seen that the product produced consists of non-uniform beaded fibers. The emergence of these beads appears to be due to an axisymmetric instability that occurs during the spinning process. In the current work, we propose an approach to predict the axisymmetric stability behavior of highly conducting jets of PEO/water solutions. The study follows on from a previous paper (Carroll and Joo, 2008) where the axisymmetric instabilities of low electrical conductivity PIB Boger fluid jets during electrospinning were considered.

Solutions of poly(ethylene oxide) (PEO) in water are very commonly used as a model system for electrospinning studies. Experimental electrospinning studies using PEO/water have been carried out by Jaeger *et al.* (1996) and Son *et al.* (2004). Both papers report that, under certain conditions, beaded fiber products are obtained, whereas under different spinning conditions, the fibers observed are seen to be uniform. PEO based solutions were also used by Reneker *et al.* (2000) studying the whipping instability seen in electrospinning. In their work, a relatively high concentration (~6 wt%) of comparatively low molecular weight (~400 k) PEO is used, which appears to favor the emergence of whipping rather than axisymmetric instabilities.

Hohman *et al.* (2001) consider PEO/water solutions during their theoretical analysis of the competition between whipping and axisymmetric modes during electrospinning. In their analysis, they identify an axisymmetric 'conducting instability mode' that is separate from the typical capillary-driven Rayleigh instability. In a recent work, Yu *et al.* (2006) electrospun a series of PEO/water solutions and performed an analysis of how the Rayleigh instability within

*Corresponding author: ylj2@cornell.edu

Table 1. Physical properties of PIB/PB and PEO/water fluids

Fluid	Relaxation time, λ	Electrical conductivity, K	Surface tension, γ	Total zero shear viscosity, η_o	Viscosity ratio, $\beta=\eta_s/\eta_o$
	[s]	[S/m]	[N/m]	[Pa.s]	[-]
PIB/PB	0.006	3.0×10^{-4}	1.46×10^{-2}	0.175	0.274
PEO/water	0.20	1.4×10^{-2}	6.80×10^{-2}	1.0	10^{-3}

Table 2. Typical values of key dimensionless numbers for two fluids

	$Pe=\frac{2\bar{\varepsilon}_D v_o}{KR_o}$	$\mathrm{Re}=\frac{\rho v_o R_o}{\eta_o}$	$We=\frac{\rho v_o^2 R_o}{\gamma}$	$\varepsilon_E=\frac{\bar{\varepsilon}_D E_o^2}{\rho v_o^2}$	$De=\frac{\lambda v_o}{R_o}$	$E_x=\frac{(\Delta V/d)}{E_o}$
PIB/PB	2.5×10^{-3}	5.15×10^{-3}	1.31×10^{-4}	8.67	0.0265	1.33
PEO/water	9.12×10^{-9}	1.27×10^{-3}	5.63×10^{-5}	9.89×10^{-6}	1.44	396

the jets is stabilized by the build-up of viscoelastic stresses due to the stretching of the polymer during spinning.

In the current paper, a model for the initial stable jet seen during electrospinning (Carroll and Joo, 2006) is used to establish a jet 'base state' far from the spinneret nozzle. An axisymmetric perturbation is then introduced into this base state, and a linear stability analysis is performed to determine the expected growth rate of the axisymmetric 'beads', as well as the expected bead wavenumber. In the experimental section of the paper, highly conducting, viscoelastic PEO/water solutions are prepared, characterized and electrospun, and the jet behavior observed is captured using high-speed photography. The jet stability characteristics are then compared with the theoretical predictions.

2.1. Experimental

In the current paper we work mainly with a 2.5 wt% solution of PEO (Aldrich, $M_w=2\times10^6$) in water. Extensional relaxation times of similar fluids were measured by Theron *et al.* (2004) to be ~200 ms. The fluid conductivity was measured using a conductivity meter (VWR model 2052). The fluid properties of PEO/water solution are summarized in Table 1. Those of 8000 ppm PIB/PB Boger fluid are also shown in the Table for comparison.

A conventional electrospinning setup for polymer solutions equipped with a high speed camera is used for the current study. During spinning, a digitally controlled syringe pump (Harvard Apparatus, PHD 2000) pumps fluid out of a syringe nozzle at a known rate (usually order 0.1 mL/min or less). The syringe needle is connected to a high voltage source (Gamma High Voltage Research, ES-30P), which causes a large potential difference to exist between the nozzle and the grounded aluminium collector plate. The distance between the syringe tip and the collector plate, d, is typically 15 – 30 cm for the PEO solutions electrospun here. The apparatus is arranged with the spinneret vertically above the collector plate. In order to capture the very rapid emergence of the instability, we employ a Redlake HS-3 high-speed camera. For the emergence of the PEO/water beads, it was found that frame rates of 1000 – 5000 frames per second were most appropriate. The image sequences obtained are processed using MotionPro Central software. Based on spinning conditions with the fluid physical properties from Table 1, the dimensionless groups required in the model can be deduced. The values of key dimensionless groups for both PIB/PB and PEO/water fluids are shown in Table 2.

2.2. Theoretical

The fluid is described as a leaky dielectric with charges only on the jet surface and viscoelastic models for polymer solutions such as Oldroyd-B and FENE-P are fully coupled with the fluid momentum equations and Gauss's law. A theoretical model for the jet is derived using a thin filament approximation, and the resulting differential equations governing electrically charged, stable polymeric jets are solved numerically (Carroll and Joo, 2006). An axisymmetric perturbation is then introduced into this base state, and a linear stability analysis is performed to determine the expected growth rate of the axisymmetric 'beads', as well as the expected bead wavenumber. More specifically, we use the dispersion relation to work out the expected instability growth rates, ω, as a function of wavenumber, k. The dispersion relation is a quartic polynomial in ω, and there are therefore generally 4 distinct stability branches. We are principally interested in extracting the maximum ω value, and the wavenumber, $k_{critical}$, at which this occurs. This is the instability that should emerge fastest and dominate in practice, and the values obtained using the analysis can be directly compared with the experimentally-observed growth

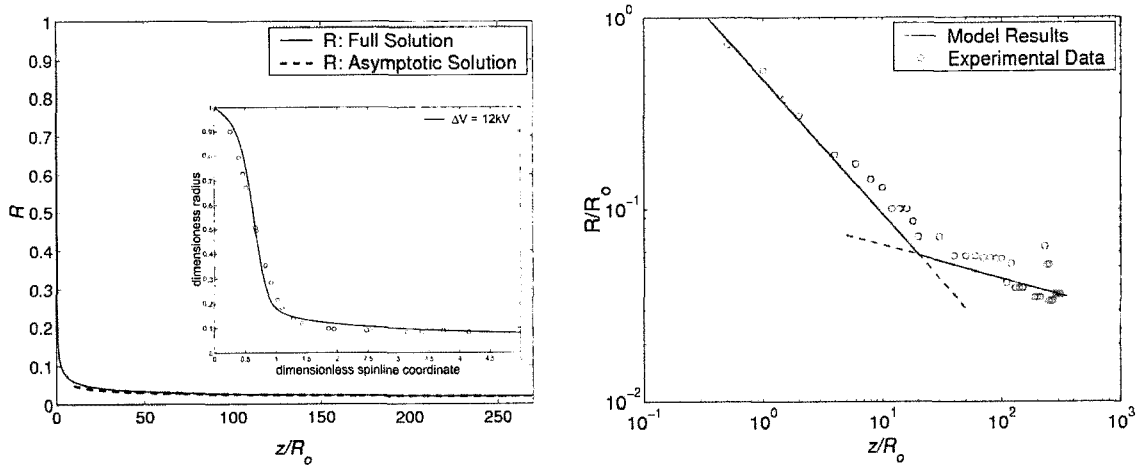

Fig. 1. Stable jet profiles. *Left*: PIB/PB Boger fluid (The inset is the comparison with experimental data near the spinneret.), *Right*: Simulation and experimental data for PEO/water solution.

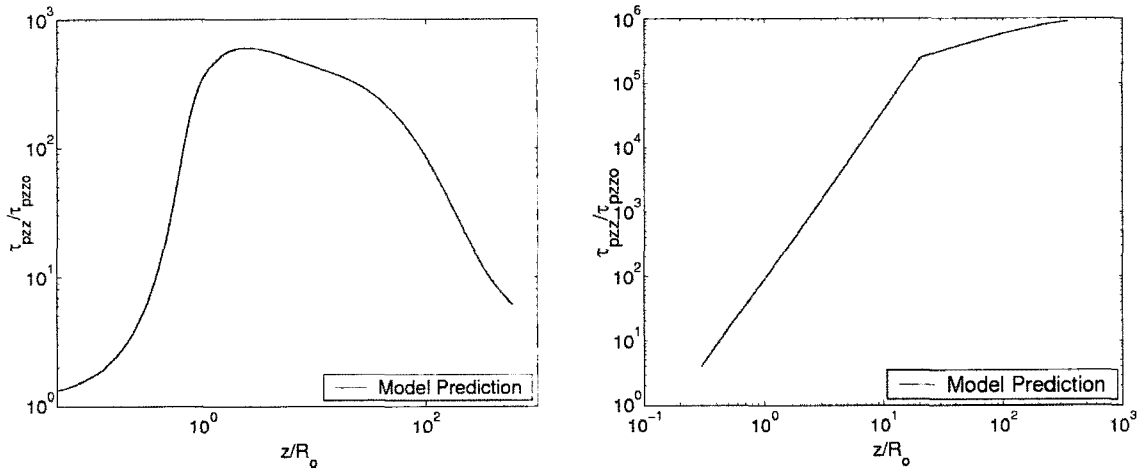

Fig. 2. Evolution of axial polymeric stress profiles along the spinline. *Left*: PIB/PB Boger fluid, *Right*: PEO/water solution.

rates and wavenumbers. We refer the reader to our recent publication for more details on the stability analysis (Carroll and Joo, 2008).

2.3. Results and discussions

2.3.1. Stable jet profiles

The stable jet radius profiles for both PIB/PB and PEO/water solutions are shown in Fig. 1. The results from the asymptotic analysis with solutions of the full stable jet governing equations are shown for the PIB/PB Boger fluid (see Carroll and Joo, 2008). We note that for the highly conducting, viscoelastic PEO/water solution the visoelastic force as well as the inertial force needs to be included to balance the electrical force term in the final boundary condition. The difference in the evolution of the viscoelastic stress of two fluids along the spinline is shown in Fig. 2. It is predicted that the viscoelastic stress for the PIB/PB Boger fluid is relaxed as the jet moves far away from the spinneret, while that of the highly viscoelastic PEO/water solution steadily increases with increasing the distance from the spinneret.

2.3.2. Linear stability analysis

The next step in the analysis is to use the stable jet data as a basis for performing a linear stability analysis. We are principally interested in extracting the maximum ω value, and the wavenumber, $k_{critical}$. The values obtained using the analysis can be directly compared with the experimentally-observed growth rates and wavenumbers. The dispersion relation for two fluids is shown in Fig. 3. It is predicted that PIB Boger fluid has two distinct unstable axisymmetric instability modes. The first mode is the 'conducting mode' that is unstable at low wavenumber (*i.e.* long wavelength), and the growth rate is close to zero. Due to the low electrical conductivity of the PIB fluid, this mode is dominated by the other unstable mode, which is capillary-driven (Carroll and Joo, 2008). For the PEO/water solution, the maximum growth rate of the most unstable branch is $\sim 10^3\ s^{-1}$, which is very consistent with the growth rates of the beads

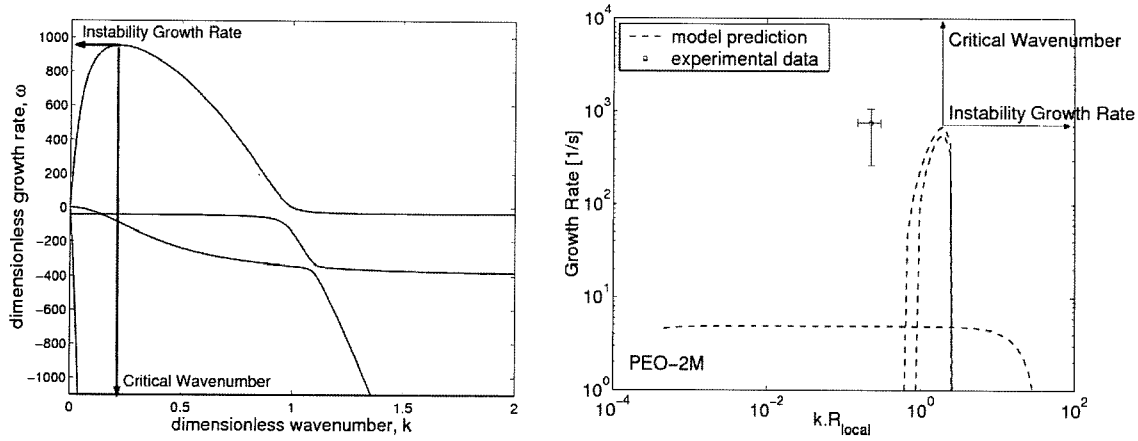

Fig. 3. Linear stability analysis results. *Left*: PIB/PB Boger fluid; *Right*: PEO/water solution.

seen experimentally for this fluid. The critical wavenumber prediction is however less accurate, possibly due to the limitations of the polymeric constitutive model. Interestingly, when the formula for the maximum expected growth rate of a capillary-driven instability (as presented by Yu *et al.* (2006)) is used for this case, the growth rate predicted is of order ~10 s^{-1}. This is much lower than the order 10^3 s^{-1} value seen experimentally and predicted by the linear stability analysis used here. This strongly suggests that the instability observed for the PEO/water fluid is driven by forces other than capillary action. The emergence of this new branch for PEO/water fluid is examined in more detail using an energy analysis approach in the next section.

2.3.3. Energy analysis

In this section, energy analysis similar to that performed by Joo and Shaqfeh (1994) is then conducted to examine what is driving the growth of the axisymmetric instability.

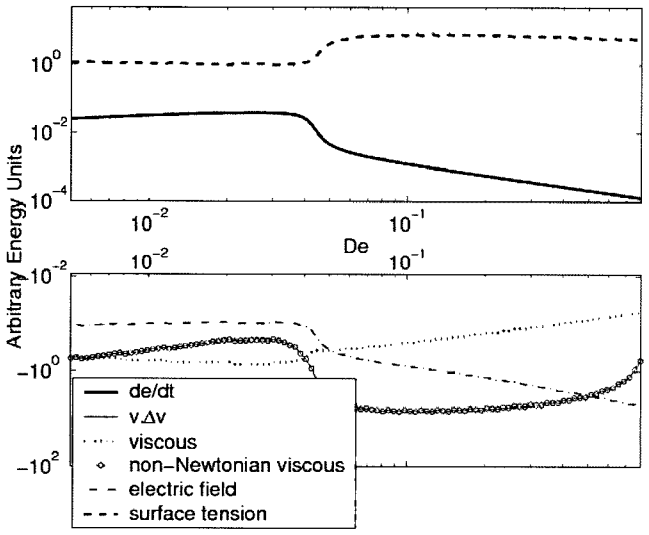

Fig. 4. Energy analysis results for low conductivity PIB Boger fluid. It is seen that the instability is driven solely by surface tension (the net growth of the instability is represented by *de/dt*).

In order to do this, multiplying the order δ jet momentum equation across by the velocity perturbation v_ε to get a disturbance energy equation, and then integrating across a complete wave cycle. The various terms in the resulting equation can easily be identified as being due to surface tension/Newtonian viscous effects/non-Newtonian viscous effects *etc.* It is then examined which of these terms are feeding energy into the instability (*i.e.* driving the instability), and which terms are stabilizing.

During the analysis of the axisymmetric instability observed during the electrospinning of PIB Boger fluid, it was seen that the instability was solely driven by surface tension (see Fig. 4). For the case of the PEO/water solution however, the situation is different due to the fact that the solution exhibits a much higher electrical conductivity and viscoelasticity than the PIB fluids.

The energy analysis results for the case of PEO/water fluid are shown in Fig. 5. It should be noted that the electric field is predicted to be the dominant term driving the instability and the non-Newtonian viscous term becomes

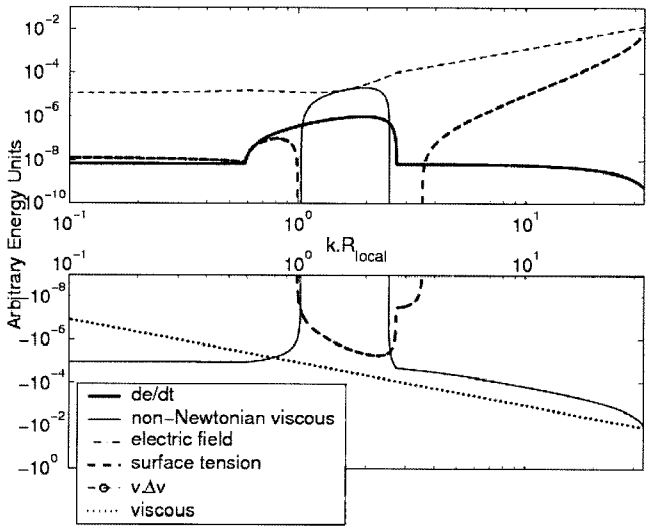

Fig. 5. Energy analysis results for PEO/water fluid.

destabilizing in the wavenumber interval $1<k.R_{local}<2.5$, rapidly pushing energy into the instability. The electric field term in the energy analysis emanates from the electric force term in the jet momentum equation. For the case of the PIB Boger fluid, the energy analysis results show that the term resulting from the coupling between the surface charge and electric field is the most important one. This term is seen to be stabilizing. For the PEO/water systems however, much larger surface charge densities are present (since the electrical conductivity is much larger and $\sigma \propto 1/Pe$). This leads to a dominant surface charge term, which is a destabilizing influence for this case. It thus appears that interaction between the charges on the jet with an aid of viscoelasticity is driving the instability.

3. Modeling of nonisothermal polymer jets in melt electrospinning

While most of previous work on electrospinning has involved polymer solutions, much progress has also been made in polymer melt electrospinning (Zhou *et al.*, 2006). The latter is more attractive for industrial applications because it is environmentally benign, it eliminates the solvent recovery and treatments costs, and there is a wider selection of polymers available, including such important systems as polyethylene (PE) and polypropylene (PP) which do not have appropriate solvents at room temperature. Besides above advantages, this solvent-free approach also opens the door to theoretical routes to model electrospinning without the complications associated with solvent evaporation.

In the current study, we extend the previous treatment by Carroll and Joo (2006) to the case of nonisothermal polymer melt jet and compare the simulation results to experiments on polylactic acid (PLA).

3.1. Experimental

The experimental setup (Fig. 6) for the current study is described in detail in our previous work (Zhou *et al.*, 2006) which includes basic components such as a micro-flow controller (PHD2000, Harvard Apparatus), a high voltage supplier (ES30P, Gamma High Voltage Research, Inc.) and a collector as well as some critical components for melt electrospinning such as a heating oven for polymer melt reservoir (T_1), a nozzle heater (T_2), a heated guiding chamber (T_3), and a temperature controllable collector (T_4). A PLA resin was obtained from Cargill-Dow which has a molecular weight around 186,000 and polydispersity of 1.76 with major L configuration. In our experiments, PLA resins were put in a 5 ml syringe and heated for half an hour in the shielded heating unit at 200°C. The micro-flow controller then fed the PLA melt through a nozzle with a flow rate from 0.01-0.1 mL/min. Temperature of the nozzle ranged from 175°C to 255°C, and the potential difference and distance between the nozzle and the collector were 5-25 kV and 10 cm, respectively. The charged melt jet was spun either with or without the heated guiding chamber before collected on an air-cooled copper collector.

Predicted simulation results are compared with experiments in two different ways. First, the initial jet radius profiles for comparison with the numerical predictions are collected by focusing a CCD camera (Panasonic WV-BD 400 with Nikon 55 mm 1:2.8 lens) on the spinneret and a section of approximately $10R_0$ into the spinning region. For best image quality, the aperture of the lens was reduced to its minimum and rear illumination was provided by a 60 W lamp. The images were digitized using Studio DC10 Plus imaging software. Secondly, the experimental measurements of the final fiber diameters resulting from thinning only in the stable region (no thinning due to whipping motion) were compared with predicted final stable jet diameter. The guiding chamber temperature was reduced to below the glass transition temperature of PLA (25-80°C), so that fiber solidification takes place in-flight prior to the onset of the whipping motion. To verify the suppression of the whipping motion of the PLA melt jet during electrospinning, a high speed camera (MotionPro HS-3, Redlake) was utilized to record a close-up high speed (1000 to 5000

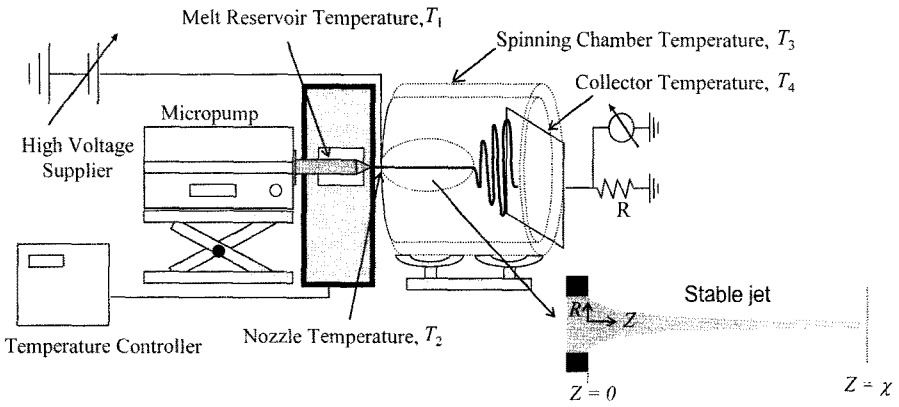

Fig. 6. Schematic of the melt electrospinning setup.

frames per second) movie of the PLA melt jet near the collector at various spinning temperatures. The resulting fiber mat is then inspected in a LEICA 440 scanning electron microscope (SEM) and the images are analyzed to determine the fiber size and distribution.

3.2. Theoretical

We have developed a model for non-isothermal, free surface flows of electrically charged viscoelastic fluids in the stable jet region of the melt electrospinning process. The model is based on thin filament approximation applied to fully coupled momentum, continuity, and energy equations, Gauss' law, and the non-isothermal Giesekus constitutive model. We have developed a new asymptotic jet thinning relationship for polymer melts particularly under non-isothermal conditions where the tensile force balances the tangential electric force. The resulting system of equations is solved numerically. We refer the reader to our recent publication for more details on nonisothermal modeling of electrospinning (Zhmayev *et al.*, 2008).

3.3. Results and discussions

To validate our nonisothermal model, simulations are compared to results of PLA melt electrospinning in two different ways. First, the simulated initial jet profiles are compared to digitized experimental images of the stable melt jet near the spinneret. Secondly, the predicted effects of melt temperature, flow rate, and electric field strength on the final jet diameter are compared to the final average fiber diameter from non-isothermal experiments where the whipping motion is suppressed by rapid cooling.

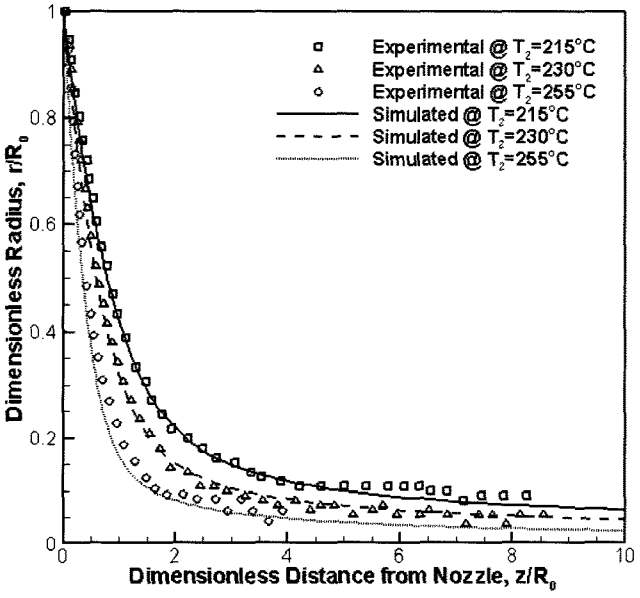

Fig. 7. Comparisons of simulated and experimental initial jet profiles at various melt temperatures, T_2=215°C, 235°C, and 255°C. We kept T_3=25°C, E=2.0 kV/cm, and Q=0.05 ml/min for all three cases.

3.3.1. Comparison of initial PLA melt jet profile

The simulated initial jet profiles are compared to digitized experimental images of the stable melt jet near the spinneret. As shown in Fig. 7, the agreement is good throughout the initial rapid thinning region for various nozzle spinning temperatures. It is interesting to note that even the current 1-D model is accurately capturing the initial jet development under various nonisothermal conditions.

3.3.2. Comparison with final average fiber diameter

Fig. 8 shows the effect of nozzle temperature T_2 on the final jet diameter for both simulation and PLA melt electrospinning experiments. The micrograph images of collected PLA fibers are also shown as insets. We note that the average fiber diameter from experiments in Fig. 8 is much larger than that of typical melt electrospun fibers because the additional thinning by the whipping motion was suppressed by low spinning temperature. Under these processing conditions, it is observed that average fiber diameter is close to the predicted final stable jet diameter and both predicted final jet diameter and average diameter of collected PLA fibers decrease, as nozzle temperature increases. It is observed that the increase in nozzle (melt) temperature decreases the viscoelasticity (and viscosity), and thus the final jet gets thinner with increasing nozzle temperature. The predicted final jet diameter and average fiber diameter from experiments at various flow rates and electric field strengths are also shown in the figure. As the flow rate decreases and the electrical field strength increases, both predicted final jet diameter and average diameter of experimentally collected fibers decrease.

4. Control of nanoparticle location via confined assembly of block copolymers during electrospinning

Controlling the spatial location of nanoparticles (NPs) in polymer matrices is the fundamental challenge surrounding the development of high end polymer nanocomposite materials. High particle surface energies and strong interparticle interactions often lead to the aggregation of particles making it difficult to control their location. One can use block copolymers (BCP) as templates for guiding the location of nanoparticles for sophisticated tailoring of the overall nanocomposite properties (Balazs *et al.*, 2006).

Although surface modification has played an important role in guiding NPs at desired locations in block copolymers for many metals like gold and silver, in case of magnetically active particles like magnetite, strong magnetic dipole interactions between particles often lead to clustering and aggregation (Harris *et al.*, 2003). Magnetite can display high saturation magnetization and resistance to oxidation, attracting great interest in electrical and biomedical applications. Park and Char (2006) exploited the selectivity of film casting solvents to control the morphology of mag-

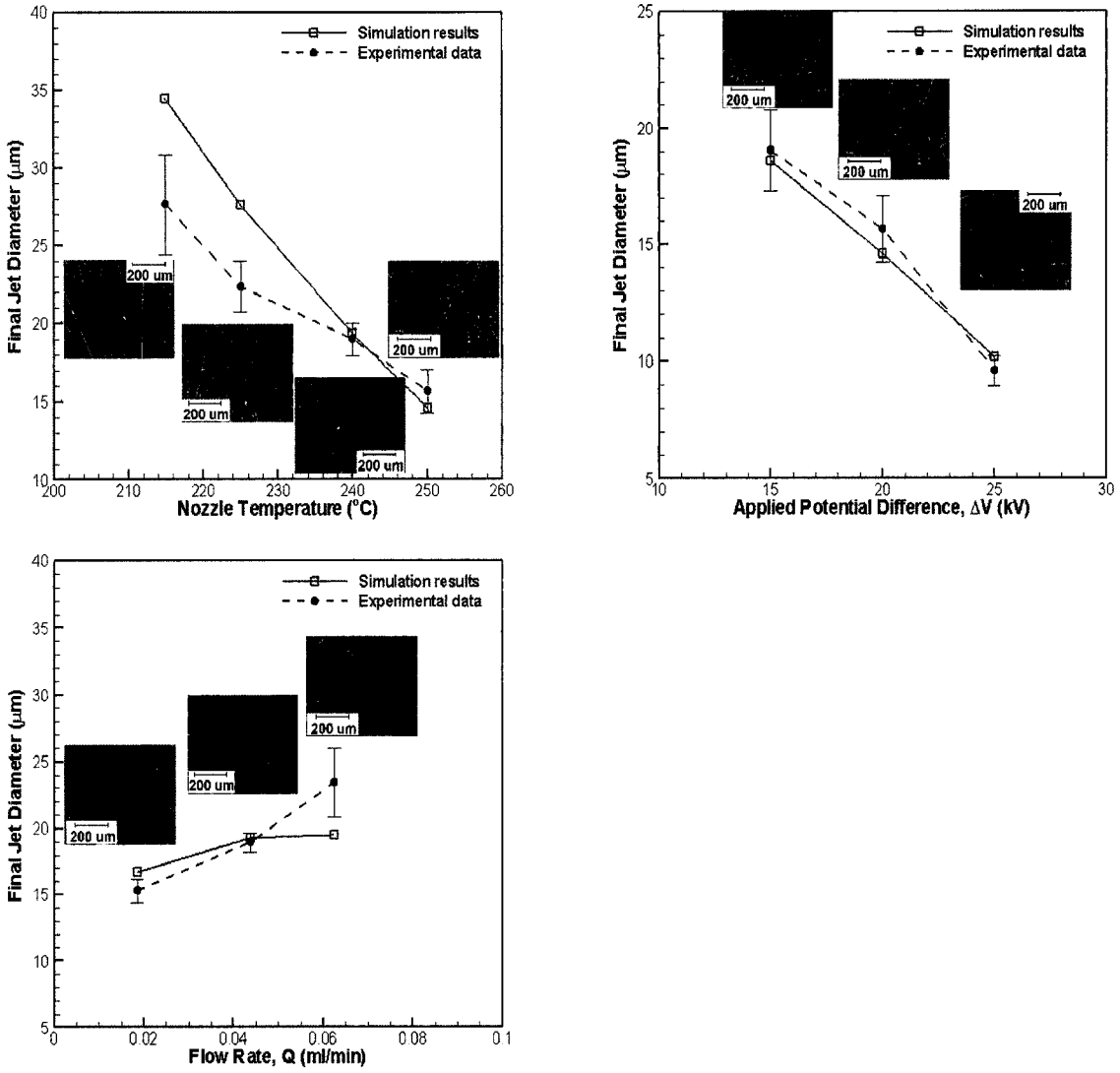

Fig. 8. Effect of nozzle temperature, applied voltage, and flow rate on fiber diameter. The simulated final fiber diameter and average diameter of collected PLA fibers are plotted at various nozzle temperatures, applied voltages, and flow rates.

netic nanoparticle/poly(styrene-*block*-isoprene) (PS-*b*-PI) nanocomposite films. For solvents like THF and toluene which are neutral for PS and PI, they reported the formation of lattice like NP aggregates inducing a BCP phase transition from cylindrical to spherical morphology. In contrast, for PI selective solvents like hexane, NPs were selectively incorporated into the PI phase for up to 5 wt% nanoparticles in neat BCP. For higher particle loading, however, aggregates were formed and selectivity of NPs was lost.

Previous studies have been limited to the use of BCP cast films as particle guiding scaffolds. The objective of this paper is to use BCP nanofibers as templates to control the location of nanoparticles not only to obtain high surface area functional nanofiber mats, but also to achieve higher particle loading owing to different fabrication conditions compared to those for cast films. To this end, we have used electrospinning to incorporate magnetite nanoparticles covered with oleyl group in lamellar forming PS-*b*-PI nanofibers. Electrospinning is a simple and versatile method that uses strong electric field to draw polymer solutions or melts to produce ultra thin fibers with diameters ranging from 50 to 500 nm. Recently, we reported the formation of highly ordered lamellar morphology in pure BCP electrospun fibers encapsulated with silica shell using coaxial electrospinning. Thermally stable silica shell allowed us to anneal the fibers above glass transition temperature of BCP and obtain equilibrium morphology (Kalra *et al.*, 2006a; 2006b). Lamellar structures in the form of stacked discs and alternate concentric rings of PS and PI are formed owing to the elongational deformation during electrospinning and cylindrical confinement of the BCP. The work on confined assembly in nanofibers is scientifically interesting, but from the material applications perspective, it is extremely important to be able to functionalize them. In the present work, we have demonstrated how to utilize con-

fined assembly to effectively functionalize these fibers with magnetic nanoparticles to develop materials for novel applications such as magnetic storage media, catalysis and bioseparations. We show that due to the inherent fast evaporation and strong deformation rates in the electrospinning process, the particles preferentially wet the PI domain and yet remain very monodisperse for much higher particle fractions than in BCP/magnetic NP films.

We also present molecular dynamics simulations coupled with a dissipative particle dynamics thermostat to model and simulate the behavior of symmetric diblock copolymer/nanoparticle systems under simple shear flow. We consider self-attracting nanoparticles to mimic magnetites used in the electrospinning study. The aim of our present study is to understand how the self-attracting nanoparticles disperse in a block copolymer system under shear flow and how the presence of nanoparticles affects the rheology, structure and flow behavior of block copolymer systems.

4.1. Experimental

PS-*b*-PI with M_{PS}=53500 g/mol and M_{PI}=70000 g/mol is synthesized using a two step living anionic polymerization (Kalra *et al.*, 2006a). The polydispersity of the polymer obtained by gel permeation chromatography is 1.04. Transmission Electron Microscopy (TEM) and small angle x-ray scattering (SAXS) studies were carried out to show the formation of lamellar morphology in films of PS-*b*-PI cast in THF. Monodisperse 4.1±0.55 nm magnetite nanoparticles with surface coated with oleyl group were synthesized using a method similar to the one demonstrated by Sun and Zeng (2002). 2 mmol of Iron (III) acetylacetonate ($Fe(acac)_3$) was mixed in 20 ml of octadecene with 1,2-hexadecanediol (10 mmol), oleic acid (6 mmol), and oleylamine (6 mmol) under nitrogen and heated to 285 °C for 30 min (ramping rate: 3°C/min). The precipitated magnetite nanoparticles by cooling were recovered by centrifugation. The presence of oleyl group on the surface of particles makes them marginally selective towards PI phase of the BCP. Coaxial nanofibers were electrospun using 15-17 wt% solution of PS-*b*-PI/Fe_3O_4 NP mixtures in THF as the inner core and silica sol gel precursor as the outer solution. NP weight fractions in solid polymer were varied from 0-10%. The volumetric flow rates used for inner and outer solutions were 0.02 ml/min and 0.03 ml/min respectively. The fibers were spun at an electric potential of 20 kV with spinneret to collector distance of 4 inches. We refer the reader to our recent publications for a more detailed overview of the experimental setup (Kalra *et al.*, 2006b). The diameters of coaxially spun fibers range from 300 nm to 1 μm as examined by Scanning Electron Microscopy (SEM) (Leo 1550) with the core diameter typically ranging from 200-500 nm. Fibers, embedded in epoxy matrix, were microtomed into 60 nm thin cross-sectional and longitudinal sections at room temperature using Leica ultracut UCT. Fiber sections were stained in osmium tetraoxide vapors for 10 min and were viewed under Tecnai T12 transmission electron microscope operated at 120 KV for further characterization.

4.2. Theoretical modeling and simulation

Coarse-grained Molecular Dynamics has been used to simulate the motion of self-attracting NPs in block copolymer and homopolymer melts. We refer the reader to our recent publication for more details on the simulation method (Kalra *et al.*, 2008). The copolymer and homopolymer chains in the current study are modeled as fully flexible bead-spring chains where the monomers are never allowed to overlap. Since we are dealing with a diblock copolymer, the chains consist of "*A*" and "*B*" blocks of monomers. The excluded volume interactions between the *A* and *B* monomers are accounted for by the purely repulsive, cut and shifted, Lennard-Jones (LJ) potential which is often referred to as the WCA potential. We use a slight modification of the Lennard Jones potential (refer to equation 4 in Kalra *et al.*, 2008) to model interactions between different components of each system studied. Equation 4 generates an attractive potential tail for all non zero *k* values. Table 3 gives details of potentials for three systems studied in this paper. Polymers are modeled as flexible bead- spring chains with a FENE (Finitely Extensible Nonlinear Elastic) potential and shear is implemented using Lee Edwards Periodic Boundary Conditions with the SLODD algorithm. To incorporate the physics of microscopic phase separation between the *A* and *B* species, we utilize an attractive potential between like monomers (*i.e.*, *A-A* or *B-B*). This interaction taken together with the repulsive *A-B* potential ensures that phase separation will occur if the temperature is below the order-disorder transition temperature. We use the same attractive potential that was used by Horsch and coworkers to model the equilibrium properties of diblock copolymer melts. In modeling the nanoparticles, we mimic the work that was recently reported by Schultz *et al.* (2005). They used a "discontinuous" molecular dynamics (DMD) technique to first

Table 3. Summary of interactions in systems studied. For a block copolymer nanocomposite *A* and *B* denotes two different monomeric beads and *P* denotes the nanoparticle

I	Block Copolymer	k=0	*A-B,B-P*
		k=0.5	*A-P,A-A, B-B*
		k=1.0	*P-P*
II	Homopolymer	k=0	*A-P, A-A, P-P*
III	Homopolymer	*k*=0	*A-P, A-A*
		k=0	*P-P*

Table 4. Simulation parameters used in the study

Parameters	Symbol	Value (MD units)
Temperature	k_BT	1
NP,monomer size	σ_P, σ	1
NP,monomer mass	m	1
Chain length	N	10
Bead density	ρ	0.85
Cubic box size	L	26-36
NP fraction	ϕ_P	0.1
Number of chains	M	1341-3600
Flory Huggins parameter*N^{20}	χN	53.3
MD integration time step	Δt	0.01
Domain spacing	d	~9.1
Copolymer end to end distance	R_0	4.62
Shear rate	$\dot{\gamma}$	0-0.15

model the equilibrium structure of diblock copolymer melts, and then to model the equilibrium behavior of BCP/NP mixtures. In DMD, all of the interactions are repulsive and phase separation is induced by repulsive shoulders between unlike species. In our simulation methodology, to model mignetites which are selectively attractive to PI domain, the attractive potential is used for NP-NP and NP-*B* interactions, while the repulsive potential is used between *A*-*B*, and NP-*A* interactions. Finally, we used a thermostat that preserves hydrodynamic interactions, *i.e.*, the Dissipative Particle Dynamics (DPD) thermostat. The detailed simulation parameters are summarized in Table 4.

4.3. Results and discussions

Fig. 9 a) shows the TEM images of cross-section and longitudinal section of microtomed fibers that were electrospun using a solution of neat PS-*b*-PI in THF as the core material. All samples in this study use silica precursor solution as the shell material. After annealing well above the glass transition temperature of the block copolymer, alternating concentric rings of PS (unstained, light regions) and PI (stained dark regions) are formed due to the cylindrical confinement of the silica shell. For 4 wt% NPs in symmetric PS-*b*-PI (Fig. 9 b)), well-ordered alternate concentric rings of PS and PI have been shown with magnetite NPs uniformly dispersed in the PI domain. For 10-15 wt% NPs, a transition of morphology has been seen from concentric rings to a bicontinuous phase with NPs again uniformly dispersed in the PI domain (see Fig. 9 c)). It should be noted that NPs still remain uniformly and selectively dispersed in the PI phase in spite of high particle loading in BCP. Nanofiber mats with bicontinuous assembly and well dispersed NPs in one domain can be useful in fabrication of membrane materials with well connected pore structure after selective etching of the other domain.

To further understand the effect of flow on the nano-

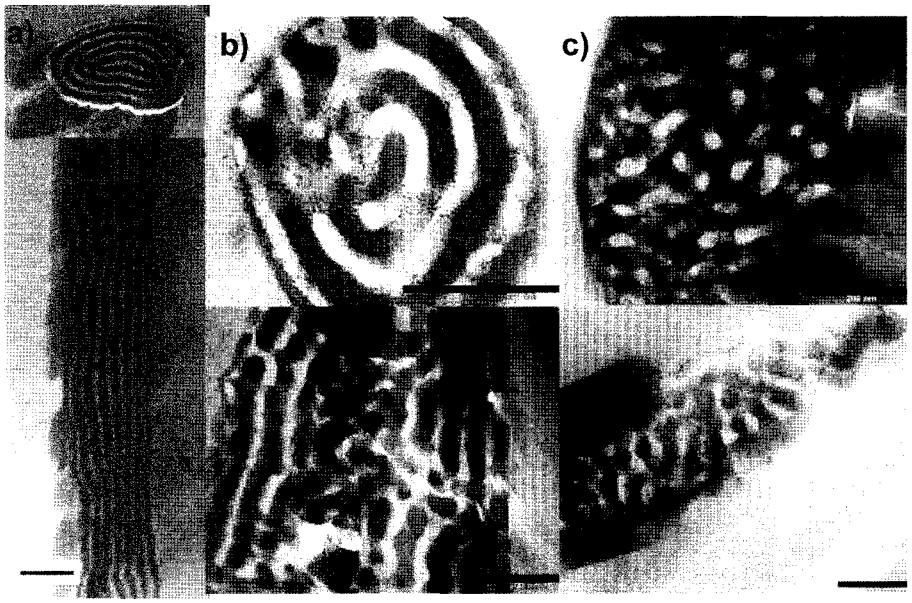

Fig. 9. TEM images of microtomed coaxial nanofibers. a) neat PS-*b*-PI, b) PS-*b*-PI with 4 wt% magnetite, and c) PS-*b*-PI with 10 wt% magnetite. Top row is the cross section, while the cut along the fiber direction is shown in the bottom row. Grey shell region is silica, in the core, light regions are PS domains, dark regions are stained PI domains and even darker dots are magnetite NPs. All scale bars are 200 nm.

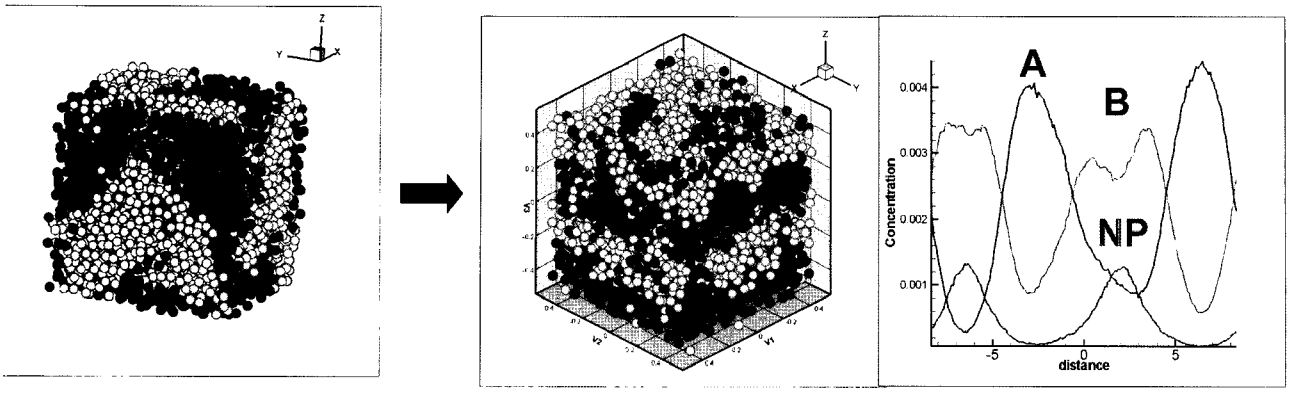

Fig. 10. Snapshots of MD simulation results for self attracting particles in BCP (system I). *left*: no shear, *middle*: shear rate=0.02, *right*: Concentration profiles for NP, *A* and *B* domains under shear.

particle location in block copolymers, we have performed coarse grained MD simulations under simple shear flow. Snapshots of MD simulation for self attracting nanoparticles in BCP (System I) without and with shear are shown in Fig. 10. The concentration profiles for NP, *A* and *B* domains under shear are also shown in the figure. As expected, self-attracting NPs with preferred interaction with the *B* domain form aggregate in the *B* domains under equilibrium, preventing symmetric BCP from assembling into lamellae. When deformation is applied, self-attracting NPs are dispersed in the *B* domain, placing themselves near the center of the *B* domain. These results suggest that deformation can play an important role in controlling the location of nanoparticles in block copolymer matrices, and that strong deformation during electrospinning can be one of the reasons why much higher particle fractions than in BCP/magnetic NP films are uniformly dispersed in the PI domain of electrospun BCP fibers.

The effect of shear can be divided into two parts; the first is the deformation that leads to an increase in the inter-particle distance and slows down the aggregation, the second is the effect of shear on diffusion constants of the nanoparticles. While the former would always work towards preventing aggregates, the latter could cause both homogenization and faster aggregation. In this case, a delicate balance of various factors such as shear rate, and interaction potentials will be required. To understand these effects of shear and provide a tool for targeted experiments, we studied a simpler case of homopolymer with nanoparticles. Furthermore, to isolate the effect of diffusion on aggregation, we use systems with different chain length of the polymer matrix. Fig. 11 shows mean squared displacement of nanoparticles vs. time curves for System II at zero shear and shear rate=0.1 MD units. As seen in the figure, the NPs diffuse at the similar rate (slope of the curve) at zero shear in spite of the large differences in the melt viscosity of different polymer chain lengths. This interesting result is in line with a previous theory which says that small particles (less than tube diameter) in a polymer melt experience the same friction as in a melt of monomer units. However, for shear rate=0.1, we find that the diffusion decreases with increasing chain length. We hypothesize that under shear flow the particles span a larger portion of the polymer chain and hence are slowed down due to the presence of entanglements. This effect of shear on particle diffusion is critical in understanding and designing an optimum well dispersed particle system. In Fig. 12, we quantify our results through the pair distribution function ($g(r)$). The initial $g(r)$ shows only one peak indicating a uniformly dispersed system. For both $N=10$ and $N=150$ polymer systems, we find that after $t=5000$ MD units, NPs in systems under shear remain much more dispersed than quiescent systems. As expected from the diffusion rates in Fig. 11, $g(r)$ for both $N=10$ and $N=150$ systems show the same trend with time at shear=0. In addition, we find that for the shorter-chain matrix, the par-

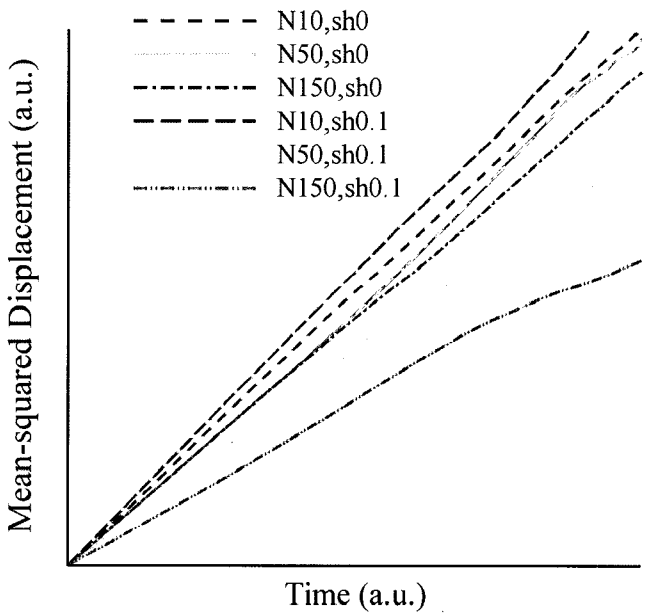

Fig. 11. Mean squared displacement of NPs vs. time for System II for different chain length(N) and shear rates(sh).

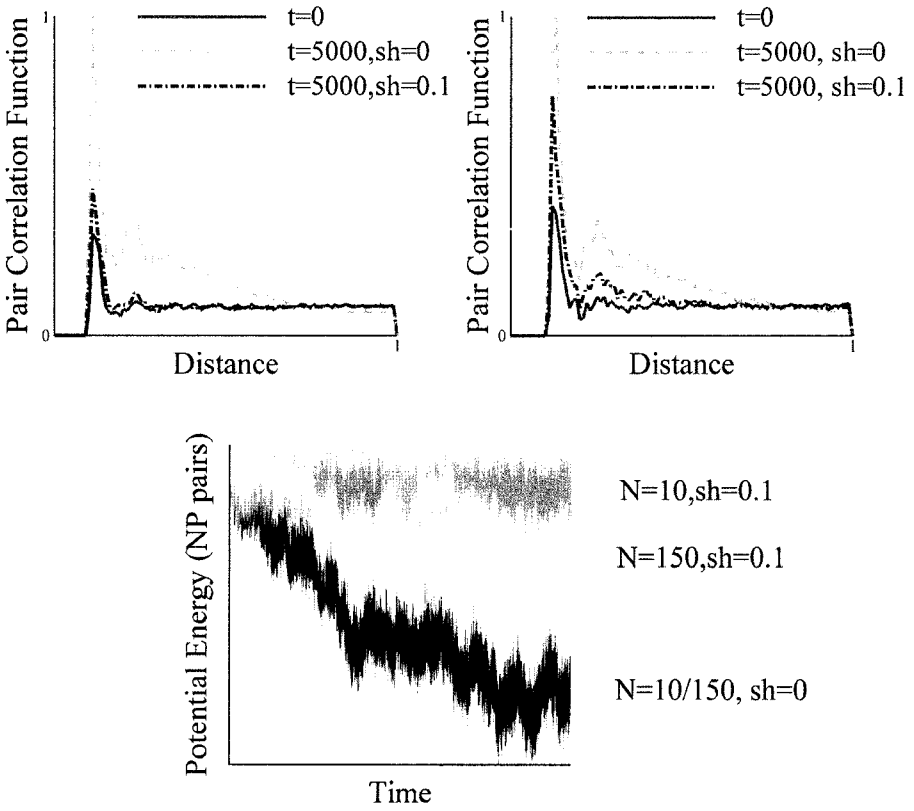

Fig. 12. System III (top left) pair distribution function of NPs in $N=10$ polymer matrix, (top right) pair distribution function of NPs in $N=150$ polymer matrix, (bottom) potential energy with time for different shear rates and chain lengths.

ticles remain more dispersed than the longer-chain matrix at shear=0.1. From these results, it is evident that faster diffusion in $N=10$ system further helps in homogenizing the system. In summary, we have conducted a study on effects of deformation on aggregation of self-attracting nanoparticles in polymer matrices using electrospinning and coarse-grained molecular dynamics simulations. We find that flow can have beneficial effects on dispersing particles and fabricate high performance nanocomposites. More rigorous comparison between electrospinning experiments and simulations based on elongational flow is currently underway.

5. Conclusions

We have presented modeling and experiments of three electrospinning systems which are i) axisymmetric instabilities in electrospinning of various polymeric solutions, ii) non-isothermal modeling of polymer melt electrospinning, and iii) control of nanoparticle distribution and location via confined self-assembly of block copolymers during electrospinning. In the first example, we have applied a linear stability analysis to electrically driven jets of highly conducting viscoelastic fluids. The results reveal that a combination of electrical (due to the interaction of charges on the jet) and viscoelastic forces during electrospinning can give rise to an axisymmetric instability and that the viscoelasticity destabilizes the flow of highly conducting fluids. The predicted axisymmetric instabilities are confirmed by electrospinning of highly conducting, PEO/water solutions. In the second example, we have extended our electrospinning modeling efforts to non-isothermal, free surface flows of electrically charged polymer melts. A new initial thinning condition based on a force balance near the nozzle for polymer melts with low electrical conductivity and high viscosity have been devised, and the simulated initial jet profiles are compared to digitized experimental images of the stable polylactic acid (PLA) melt jet near the spinneret. In addition, the predicted effects of melt temperature, flow rate, and electric field strength on the final jet diameter are compared to the final average fiber thickness from non-isothermal experiments where the whipping motion has been suppressed by rapid cooling. The last example deals with the formation of self-assembling structures of block copolymers such as PS-*b*-PI during electrospinning and utilizes such confined assembly to control the distribution and location of nanoparticles in nanofibers. Transmission electron microscopy images of microtomed electrospun fibers reveal that magnetite nanoparticles are uniformly dispersed only in one of the domains in block copolymer nanofibers. To understand how the nanoparticles disperse in a block copolymer system under flow,

coarse-grained molecular dynamics simulations coupled with a dissipative particle dynamics thermostat have been carried out. Our simulation results confirm our electrospinning experiments that deformation can be used as a parameter to effectively control nanoparticle location and distribution.

References

Balazs, A. C., T. Emrick and T. P. Russell, 2006, Nanoparticle polymer composites: where two small worlds meet, *Science* **314**, 1107.

Carroll, C. P. and Y. L. Joo, 2006, Electrospinning of viscoelastic Boger fluids: modeling and experiments, *Phys. Fluids* **18**, 053102.

Carroll, C. P. and Y. L. Joo, 2008, Axisymmetric instabilities in electrically driven viscoelastic fluid jets: modeling and experiments, *J. Non-Newt. Fluid Mech.* **153(2-3)**, 130.

Fong, H. and D. H. Reneker, 2001, "6. Electrospinning and the formation of nanofibers," in: D.R. Salem (Ed.) *Structure formation in polymeric fibers*, Munich: Hanser Gardner Publications, 225-246.

Harris, L. A., J. D. Goff, A. Y. Carmichael, J. S. Riffle, J. J. Harburn, T. G. St. Pierre and M. Saunders, 2003, Magnetite nanoparticle dispersions stabilized with triblock copolymers, *Chem. Mater.* **15**, 1367.

Hohman M. M., M. Shin, G. Rutledge and M. P. Brenner, 2001, Electrospinning and electrically forced jets: I. Stability theory, *Phys. Fluids* **13**, 2201.

Huang, Z. M., Y. Z. Zhang, M. Kotaki and S. Ramakrishna, 2003, A review on polymer nanofibers by electrospinning and their application in nanocomposites, *Composites Sci. & Tech.* **63**, 2223.

Jaeger R., H. Schönherr and G. J. Vaneso, 1996, Chain packing in electro-spun poly(ethylene oxide) visualized by atomic force microscopy, *Macromolecules* **29**, 7634.

Joo Y. L. and E. S. G. Shaqfeh, 1994, Observations of purely elastic instabilities in the Taylor-Dean flow of a Boger fluid, *J. Fluid Mech.* **262**, 27.

Kalra, V., P. A. Kakad, S. Mendez, T. Ivannikov, M. Kamperman and Y. L. Joo, 2006, Self-assembled structures in electrospun PS-*b*-PI fibers, *Macromolecules* **39**, 5453.

Kalra, V., S. Mendez, J. H. Lee, H. Nguyen, M. Marquez and Y. L. Joo, 2006, Confined assembly in coaxially electrospun block-copolymer fibers, *Adv. Mater.* **18**, 3299.

Kalra, V., S. Mendez, F. Escobedo and Y. L. Joo, 2008, Coarse-grained molecular dynamics simulation on the placement of nanoparticles within symmetric diblock copolymers under shear flow, *J. Chem. Phys.* **128**, 164909.

Park, M. J. and K. Char, 2006, Effect of the casting solvent on the morphology of PS-*b*-PI diblock copolymer/magnetite nanoparticle mixtures, *Langmuir* **22**, 1375.

Reneker D. H., A. L. Yarin, H. Fong and S. Koombhongse, 2000, Bending instability of electrically charged liquid jets of polymer solutions in electrospinning, *J. Appl. Phys.* **87**, 4531.

Son W. K., J. H. Youk, T. S. Lee and W. H. Park, 2004, The effects of solution properties on electrospinning of ultrafine poly(ethylene oxide) fibers, *Polymer* **45**, 2959.

Sun, S. and H. Zeng, 2002, Size-controlled synthesis of magnetite nanoparticles, *J. Am. Chem. Soc.* 124, 8204.

Schultz, A. J., C. K. Hall and J. Genzer, 2005, Computer simulation of block copolymer/nanoparticle composites, *Macromolecules* **38**, 3007.

Theron S. A., E. Zussman and A. L. Yarin, 2004, Experimental investigation of the governing parameters in the electrospinning of polymer solutions, *Polymer* **45**, 2017.

Yu J. H., S. V. Fridrikh and G. C. Rutledge, 2006, The role of elasticity in the formation of electrospun fibers, *Polymer* **47**, 4789.

Zhmayev, E., H. Zhou and Y. L. Joo, 2008, Modeling of nonisothermal polymer jets in melt electrospinning, *J. Non-Newt. Fluid Mech.* **153(2-3)**, 95.

Zhou, H., T. Green and Y. L. Joo, 2006, The thermal effects on electrospinning of polylactic acid melts, *Polymer* **47**, 7497.